

Supporting Information

Radical Defects Modulate the Photocatalytic Response in 2D- Graphitic Carbon Nitride

Edoardo Raciti,^{a,b} Sai Manoj Gali,^a Michele Melchionna,^b Giacomo Filippini,^b Arianna Actis,^c Mario Chiesa,^c Manuela Bevilacqua,^{d,e} Paolo Fornasiero,^{b,e} Maurizio Prato,^{b,f,g} David Beljonne,^{a,*} and Roberto Lazzaroni^{a,*}

^aLaboratory for Chemistry of Novel Materials, Materials Research Institute, University of Mons, Place du Parc 20, 7000 Mons, Belgium.

^bDepartment of Chemical and Pharmaceutical Sciences, INSTM, University of Trieste, Via L. Giorgieri 1, 34127 Trieste, Italy.

^cDepartment of Chemistry, University of Torino, and NIS Centre of Excellence, Via Giuria 9, 10125 Torino, Italy.

^dInstitute of Chemistry of Organometallic Compounds (ICCOM-CNR), via Madonna del Piano 10, 50019 Sesto Fiorentino, Italy.

^eCenter for Energy, Environment and Transport Giacomo Ciamician and ICCOM-CNR Trieste Research Unit, University of Trieste via L. Giorgieri 1, I-34127 Trieste, Italy.

^fCenter for Cooperative Research in Biomaterials (CIC biomaGUNE), Basque Research and Technology Alliance (BRTA), Paseo de Miramón 182, 20014 Donostia San Sebastián, Spain.

^gBasque Foundation for Science, Ikerbasque, 48013 Bilbao, Spain.

*Correspondence: david.beljonne@umons.ac.be; roberto.lazzaroni@umons.ac.be

S1: Experimental methodology for the EPR measurements

X-band (9.8 GHz) CW-EPR spectra were collected at 77 K on a Bruker EMX equipped with a super-high Q resonator (ER4122 SHQE). Q-band (33.8 GHz) Hyperfine Sublevel Correlation (HYSCORE) experiments were performed at 110 K on a Bruker ELEXSYS E580 using an EN 5107D2 Bruker resonator housed in an Oxford CF935 cryostat.

HYSCORE¹ is a two-dimensional experiment where correlation of nuclear frequencies in one electron spin (m_s) manifold to nuclear frequencies in the other manifold is created by means of a mixing π pulse. After 2D Fourier transformation of the time domain traces, correlation peaks are obtained, which correspond to the NMR transitions of magnetic nuclei coupled to the electron spin. The HYSCORE experiment was performed using the pulse sequence $\pi/2$ - τ - $\pi/2$ - t_1 - π - t_2 - $\pi/2$ - τ -echo was used, applying a eight-step phase cycle for eliminating unwanted echoes. Microwave pulse lengths $t_{\pi/2} = 16$ ns, $t_{\pi} = 32$ ns, and a shot repetition rate of 0.5 kHz were used. The t_1 and t_2 time intervals were incremented in steps of 16 ns, starting from 200 ns giving a data matrix of 200×200 points, while the interpulse delay τ was 144 ns. The time traces of the HYSCORE spectra were baseline corrected with a third-order polynomial, apodized with a Hamming window and zero filled. After two-dimensional Fourier transformation, the absolute value spectra were calculated. The HYSCORE spectrum was simulated using EasySpin 5.2.28 toolbox² within the Matlab 2019b software suite (The Mathworks Inc., Natick, MA) with the following spin-Hamiltonian parameters $\mathbf{g}=[2.0024]$

${}^N\mathbf{A}=[-0.6 \ -0.6 \ 1.2]$ MHz $e^2qQ/h=3$ MHz and $\eta = 0$, where \mathbf{g} and \mathbf{A} are the g tensor and the nitrogen hyperfine tensors respectively. e^2qQ/h is the quadrupolar coupling constant and η the so called asymmetry parameter which are related to the principal values Q_x , Q_y and Q_z of the traceless quadrupole \mathbf{Q} tensor by the following relations: $Q_x = -e^2qQ/4h(1-\eta)$, $Q_y = -e^2qQ/4h(1+\eta)$ and $Q_z = e^2qQ/2h$.

S2: Photocatalytic H₂ evolution

The materials were tested as photocatalysts for hydrogen production by photo-reforming of aqueous solution of ethanol (50% v/v) using a teflon-lined photoreactor illuminated with a Lot-Oriel Solar Simulator equipped with a 150 W Xe lamp and an Atmospheric Edge Filter with a cut-off at 300 nm. Co-catalyst platinum nanoparticles (Pt 1 wt%) were formed by photodeposition using Pt(NO₃)₂ as the precursor directly under photocatalytic conditions. In a typical catalytic test, 100 mg of the CN material was prior suspended in the photoreactor by sonication for 10 minutes in 80 mL of alcohol solution containing the Pt precursor and subsequently purged from air with Ar flow of 15 mL min⁻¹ for 40 minutes and thermostated at 20 °C. During the purge and the catalytic test, the materials were magnetically stirred. The on-line detection of volatile products was carried out using a Gas Chromatograph equipped with two analytical lines and a 10 way-two loops injection valve was employed for injection during on-line analysis of the gaseous products. In the former apparatus, an Agilent 7890A Gas Chromatograph equipped with a Carboxen 1010 PLOT (Supelco, 30 m x 0.53 mm ID, 30 μm film) column followed by a Thermal Conductivity Detector (TCD) was used for gaseous products quantification using Ar as carrier and a DB-225ms column (J&W, 60 m x 0.32 mm ID, 20 μm film) using He as carrier.

Four CN derivatives were used as photocatalysts for the H₂ evolution by photoreforming of ethanol in aqueous solution. Pt was employed as co-catalyst to decrease recombination rates of the photo-generated electrons and holes. Photocatalysis was investigated for times as long as 15 hours, and differences were observed across the CN catalysts in terms of H₂ formation rates. As shown in Figure SI-1, both red-CN and ox-CN could achieve higher maximum H₂ formation rates than g-CN or am-CN, confirming that the tuning of the CN structure is instrumental for the specific catalytic application. In this case, it is interesting to note that despite the smaller bandgap, am-CN is the least-performing photocatalyst, with an activity similar to that of pristine g-CN, suggesting that the presence of oxygen functional groups (ox-CN) or higher density of defects (N vacancies in red-CN) may favor the deposition and dispersion of the Pt

NPs. All samples, however, exhibit good stability over 15 hours, with no significant decline in H₂ evolution.

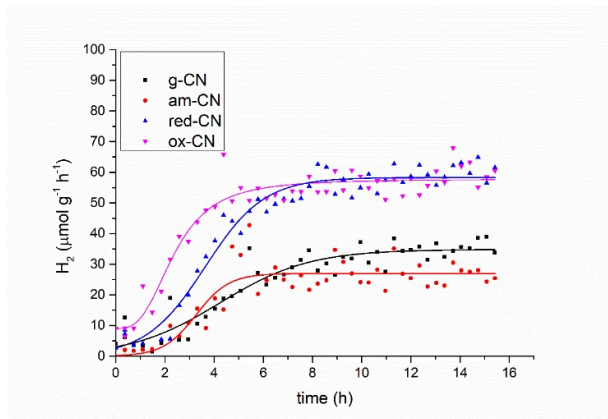


Figure SI-1: Photocatalytic H₂ evolution for various gCN forms considered in this work.

S3: Charge transfer resistance

Impedance electrochemical measurements (EIS) have been performed in a 0.1 M TBAP DMF electrolyte solution with 5.0×10^{-3} M nona-fluoro 1-iodobutane (Aldrich, purity 98%) to investigate charge transfer resistance (R_{ct}) at Open Circuit Potential (OCP) condition.

EIS measurements were performed using a frequency response analyzer (FRA, AutoLab 302 N, Metrohm) at room temperature. EIS spectra were recorded in a three-electrode thin film rotating disc electrode (TF-RDE) configuration under dark condition and with a light source (456 nm: The Kessil lamp PR160L-456 (50W)): a platinum wire was used as the counter electrode; a catalyst-coated glassy-carbon (GC) rotating disk electrode (Autolab RDE, Metrohm) with surface area of 0.196 cm² was used as working electrode; a saturated calomel electrode (SCE) was used as reference electrode, that was separated from the solution by a bridge equipped with a Vycor frit. EIS spectra (single sine measurements) were acquired at OCP under pure Ar atmosphere with a 10 mV amplitude voltage perturbation in the frequency range from 100 kHz to 0.1 Hz, at a rotation speed of 1200 rpm. The high frequency part of Nyquist plots (range of kHz) was fitted with a Randle-type Equivalent Circuit (EC) model by using Z View Software from Scribner Corporation to determine the R_{ct} parameters.

Electrochemical impedance spectroscopy (EIS) represents an interesting method to determine simultaneously different parameters concerning electron-transport processes occurring in the photo/electro/catalyst-based systems. Despite a large number of studies analyzing the electron-transport processes based on EIS measurements only under dark conditions, the result of EIS

measurements obtained in the dark and with a light source should be carried out and compared to investigate the effect on charge transfer mechanism at the interface between electrode-electrolyte .

According to the data summarized in Table SI-1, a decrease of Rct in the presence of a light source with respect to the dark condition was found for both am-CN and g-CN materials. Even if different absolute Rct values could be attributed to a different homogeneity deposition of the catalyst on the GC support, the Rct values clearly show that the charge transfer at the electrode-electrolyte interface, already occurring in dark condition, has been further improved in the presence of a light source.

Table SI-1: Charge transfer resistance (Rct) at Open Circuit Potential (OCP) condition obtained for gCN and am-gCN surfaces. Randle EC: Rel (R-CPE) applied to 800-5000 Hz, where Rel= total electrical resistance; Rct= charge transfer resistance.

System	Rel (Ωcm^2)	Rct (Ωcm^2)
am CN		
no NFIB, no light	59	670
NFIB, no light	65	165
NFIB + light	52	65
g CN		
no NFIB, no light	52	204
NFIB, no light	58	96
NFIB + light	53	23

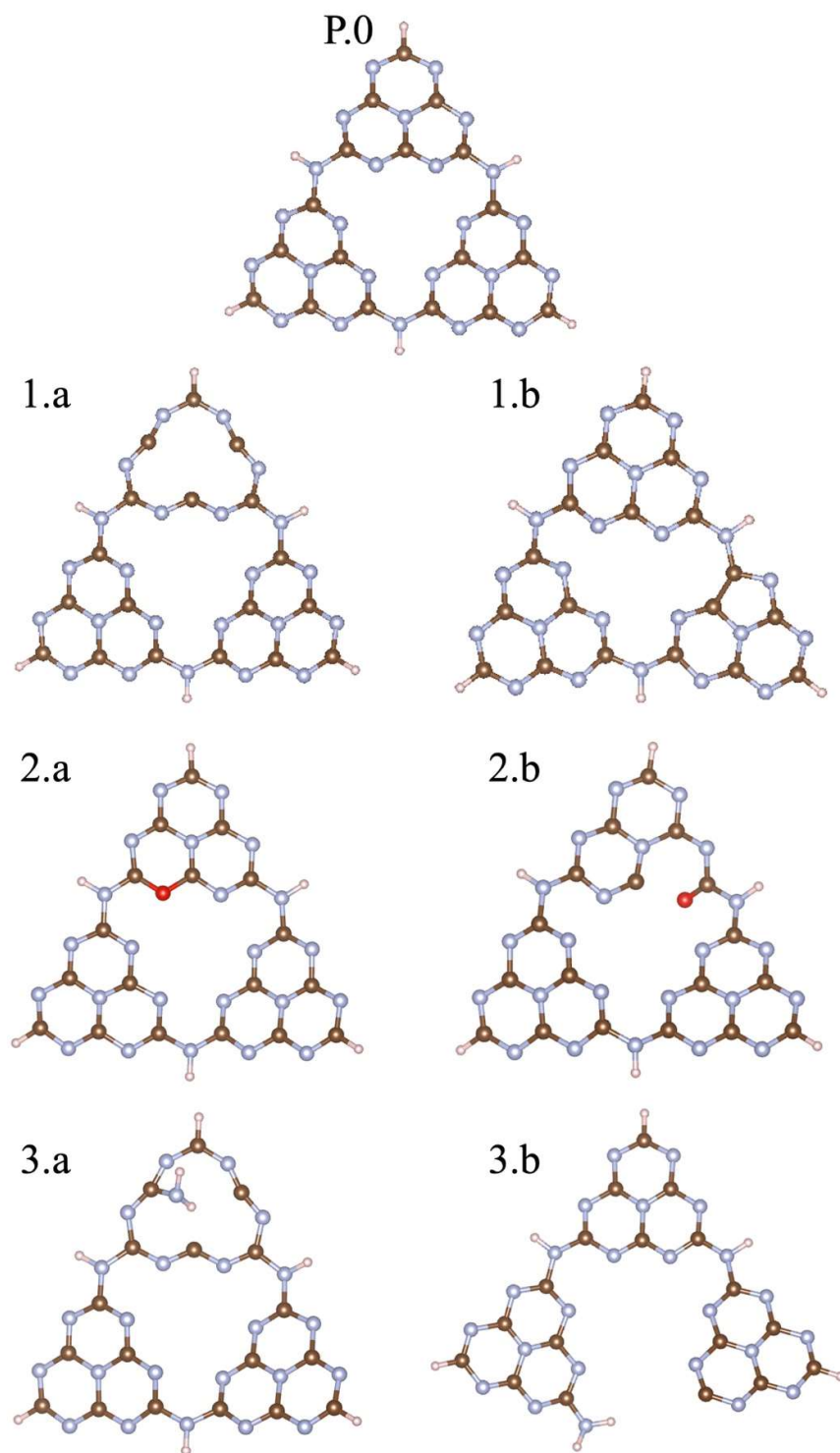
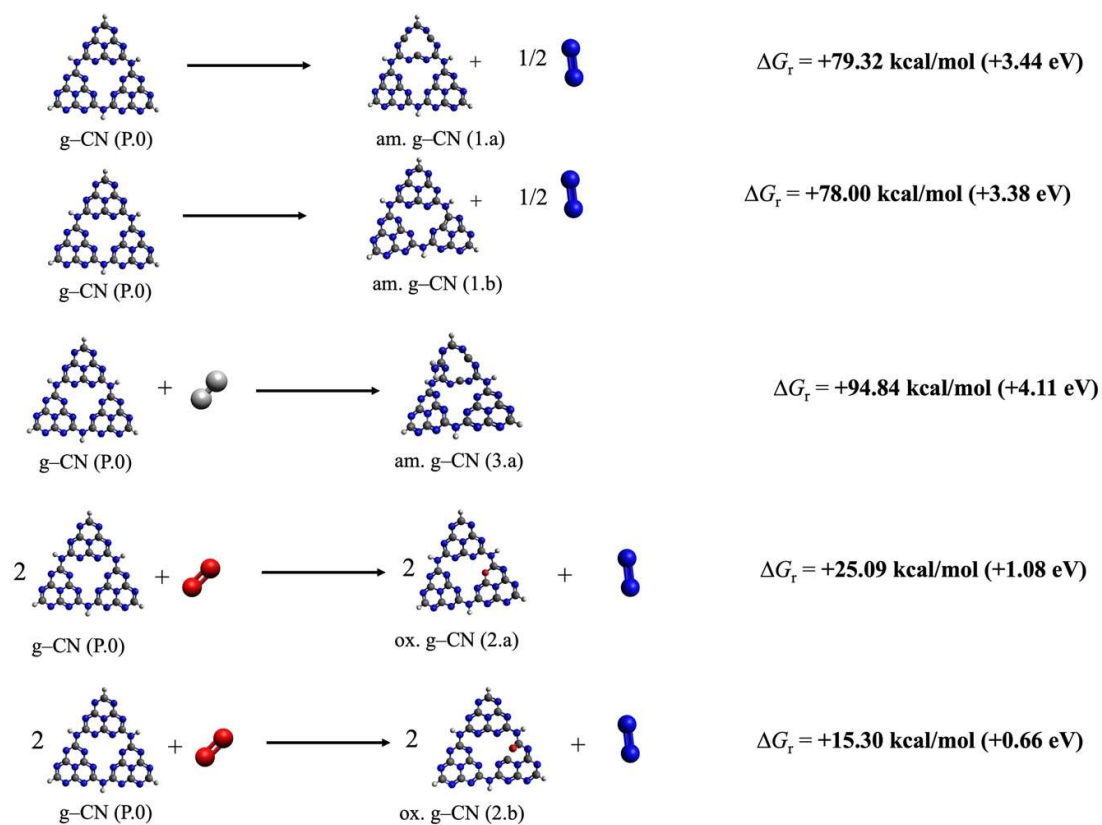


Figure SI-2: Molecular equivalents of gCN surfaces in their pristine (P.0) and defective forms (1.a/b, 2.a/b, 3.a-b,) considered in this work. gCN surfaces in their pristine (P.0) and defective forms (1.a/b, 2.a/b, 3.a-b) considered in this work (carbon: grey; nitrogen: blue; oxygen: red; hydrogen: pink). am-gCN surfaces are represented to contain nitrogen vacancies either at the center or at the edge of a heptazine unit as shown in 1.a to 1.b; oxy-gCN surfaces in their pyran-like (2.a) and carbonyl-like (2.b) forms were created by substituting the heptazine edge nitrogen vacancy. Structural defects with disconnected bonds between nitrogen and carbon atoms, either at the heptazine center or the edge, presented by 3.a and 3.b respectively, represent the red-gCN forms



System	E (eV)	
	Periodic	Molecular
1.a	4.71	3.44
1.b	4.80	3.38

Figure SI-3: Defect formation energies of all the defective gCN forms along with the schematics of the reaction mechanism considered, obtained by considering the molecular models. The defect formation energies of nitrogen vacancies (structures 1.a and 1.b), obtained using both the periodic and molecular models show a semiquantitative agreement. The slightly lower defect formation energies obtained using the molecular models for structures 1.a and 1.b compared to the periodic ones could be attributed to the comparatively larger energy gain in molecular models due to structural reorganization upon the formation of nitrogen vacancy.

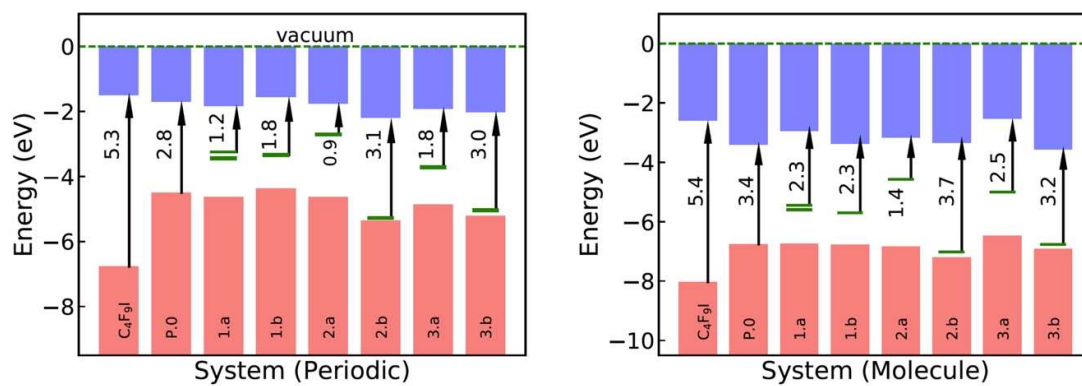


Figure SI-4: Electronic structure of (a) left: periodic and (b) right: molecular gCN forms in its pristine, radical-reduced/amorphous, radical-oxidative, radical-disconnected, along with the isolated C_4F_9I molecule. A very good agreement was observed between the periodic structures and their molecular equivalents.

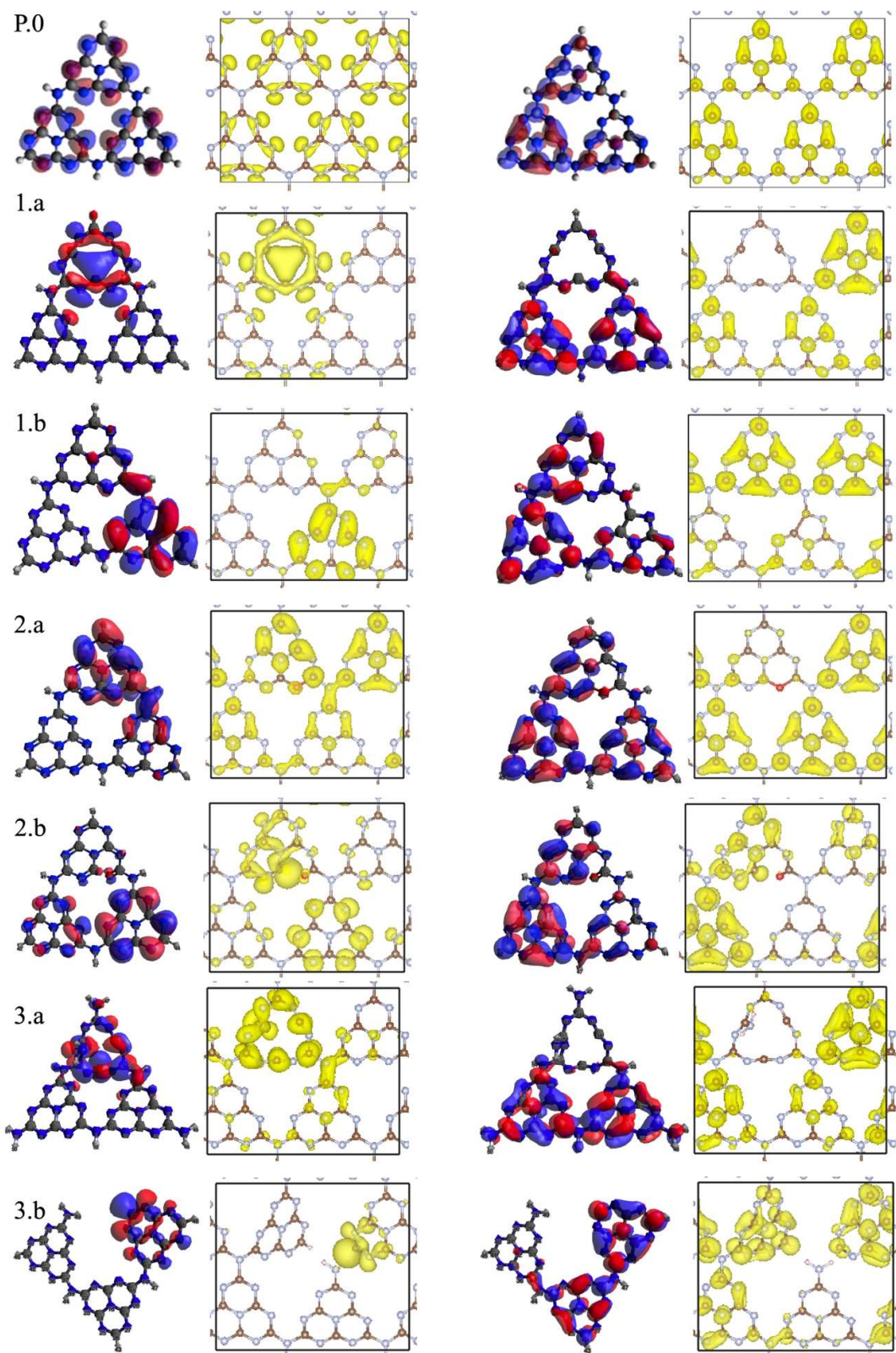


Figure SI-5: Molecular (left side of each panel) and crystalline (right side) orbitals of gCN in its pristine (P0), radical - reduced/amorphous (1.a/b), radical -oxidative (2.a/b), disconnected (3.a/b). A good agreement is observed between the periodic structures and their molecular equivalents. For clarity, only the orbitals of mid-gap defect state (HOMO, left column) and LUMO (right column) orbitals are shown.

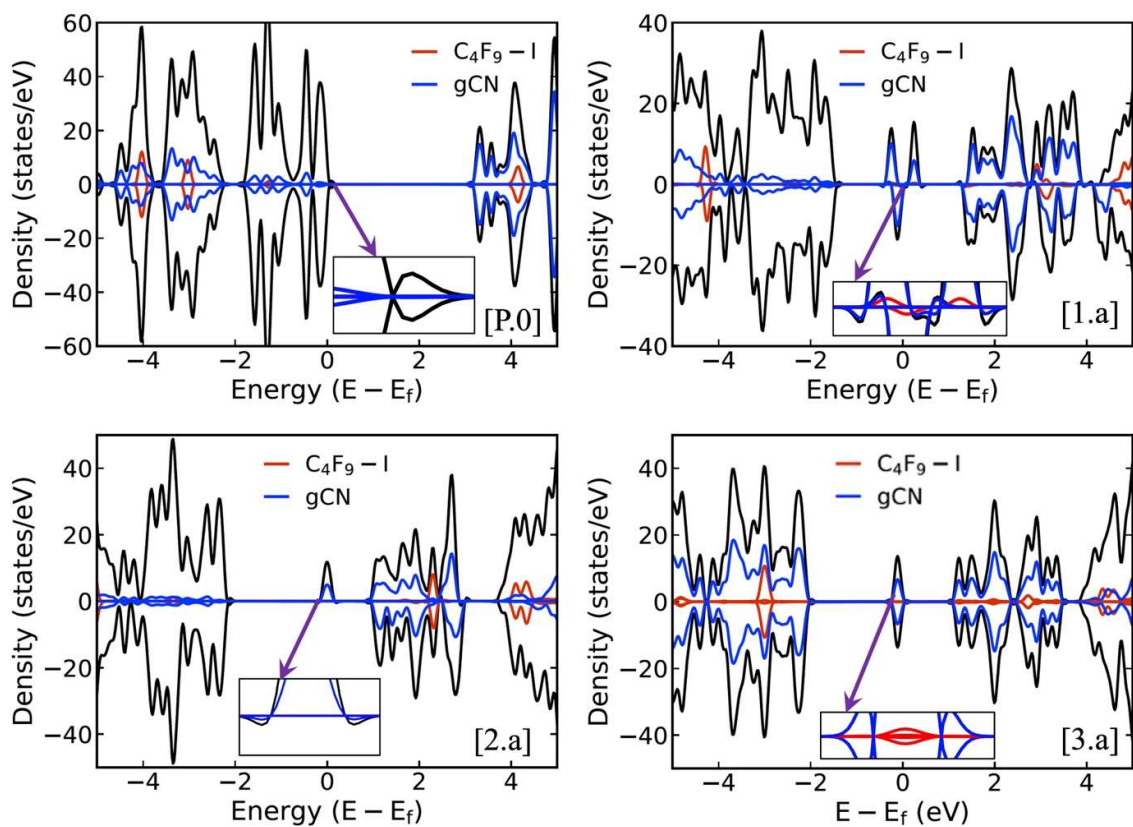


Figure SI-6: Partial density of states (pDOS) of gCN/C₄F₉-I systems with gCN structures in their (P.0) pristine form, amorphous gCN structure (1.a) with a nitrogen vacancy at the center of the heptazine unit, oxidative gCN structure (2.a) in its pyran-like form, reduced gCN structure (3.a) with disconnected nitrogen/carbon bonds at the center of the heptazine unit. Radical gCN/C₄F₉-I heterostructures show mid-gap defect states within the electronic bandgap.

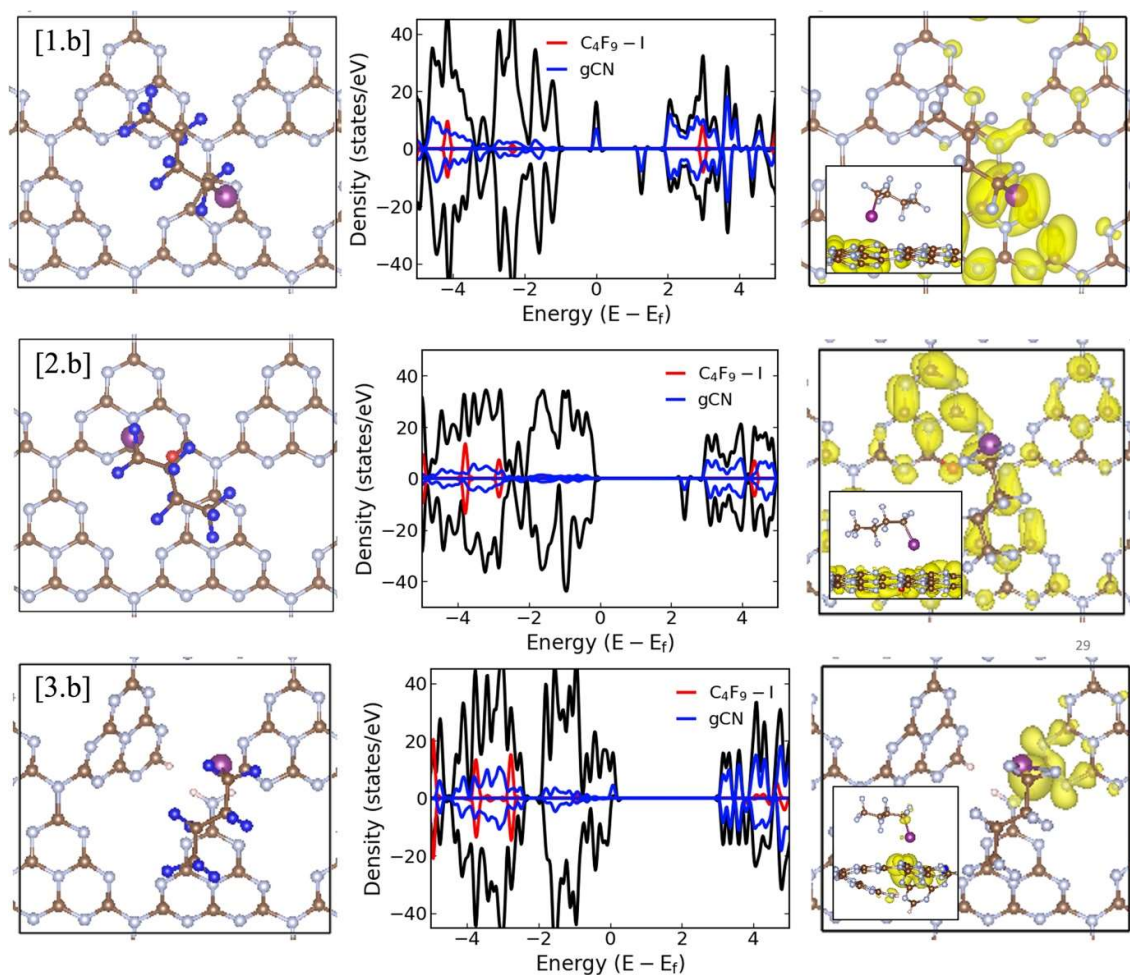


Figure SI-7: Partial density of states (pDOS) of gCN/C₄F₉-I systems with gCN structures in their amorphous gCN structure (1.b) with a nitrogen vacancy at the edge of the heptazine unit, oxidative gCN structure (2.b) in its carbonyl-like form, reduced gCN structure (3.b) with disconnected nitrogen/carbon bonds at the edge of the heptazine unit (carbon: brown; nitrogen: blue; oxygen: red; hydrogen: pink, fluorine: navy and iodine: magenta). Radical gCN/C₄F₉-I heterostructures show mid-gap defect states within the electronic bandgap. Crystalline orbitals of the mid-gap defect state are shown to the right.

Table SI-1: Adsorption energies (in kcal/mol) of the C₄F₉-I molecule adsorbed on the gCN surface in its pristine and defective forms, show a quantitative agreement between the periodic and molecular models.

System	E _{Ads} (kcal/mol)	
	Periodic	Molecular
P.0	6.10	5.51
1.a	17.4	15.6
1.b	11.2	10.5
2.a	8.14	8.10
2.b	7.06	7.21
3.a	12.5	14.5
3.b	11.4	14.2

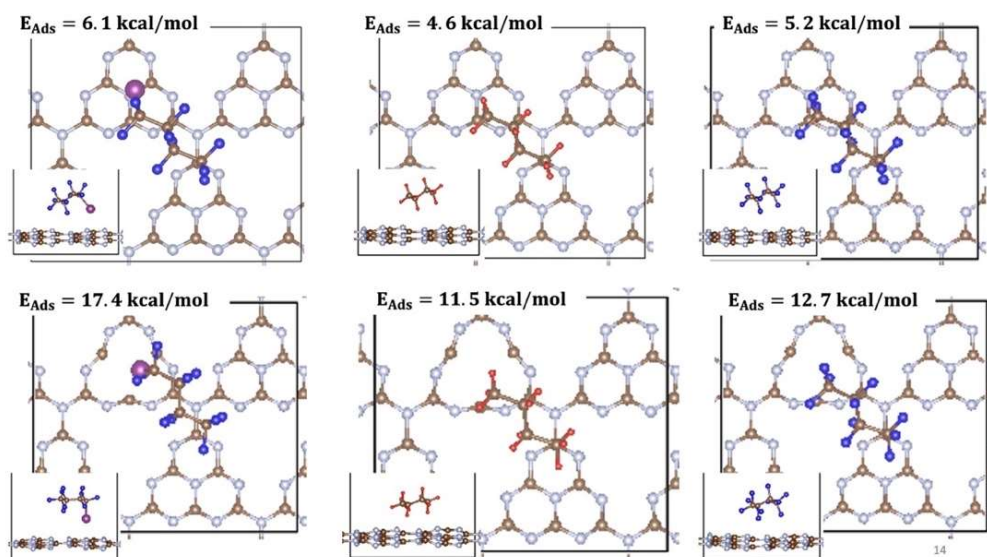


Figure SI-8: Adsorption of C_4F_9-I (left), C_4H_{10} (center) and C_4F_{10} (right) molecules on (top) pristine gCN and (bottom) a defective gCN surface containing a nitrogen vacancy at the center of the heptazine unit. Iodine, Fluorine and Hydrogen atoms are represented with magenta, blue and red colors, for clarity.

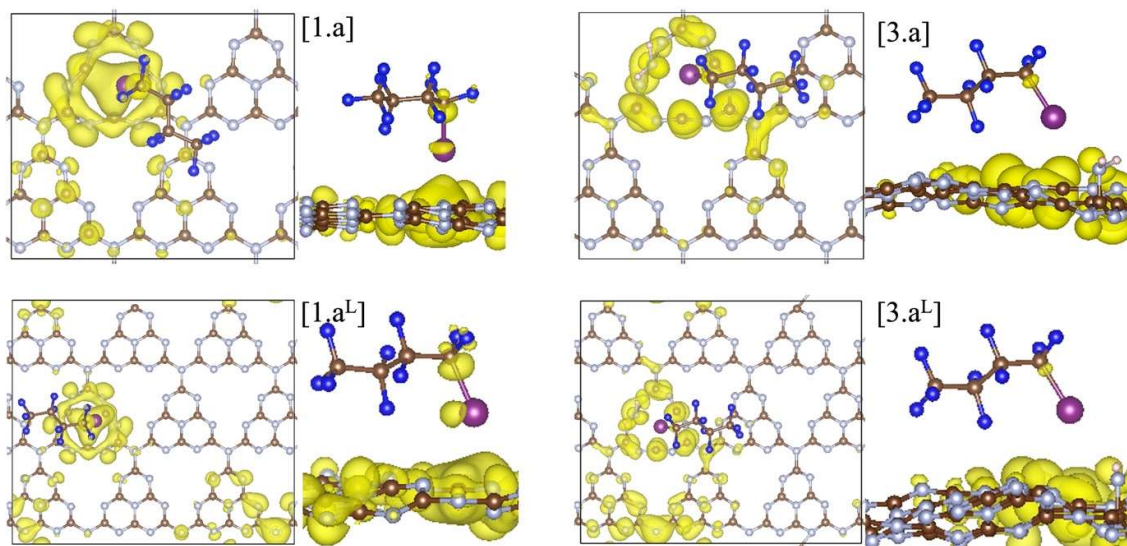
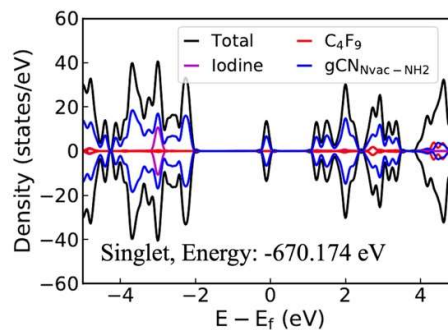
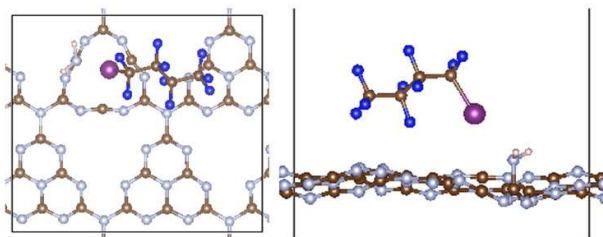
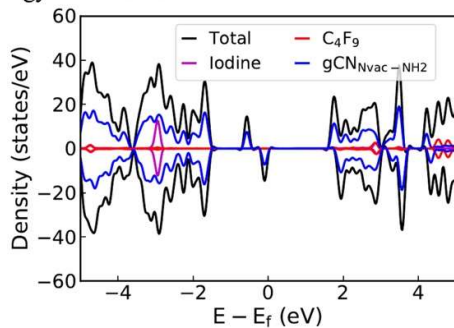


Figure SI-9: The electronic structures of C_4F_9-I adsorbed am-gCN (structure 1.a) and red-gCN (structure 3.a) for the periodic gCN surfaces replicated to (a) top: $4 \times 4 \times 1$ and (b) bottom: $6 \times 6 \times 1$, along with their molecular orbitals at the localized mid-gap state. The adsorption energies of C_4F_9-I atop the am-gCN surface (structure 1.a and 1.a^L) is ≈ 17 kcal/mol and atop the red-gCN surface (3.a & 3.a^L) is ≈ 12.5 kcal/mol.

Structure: 3.a



Singlet Broken Symmetry,
Energy: -670.431 eV



Triplet, Energy: -669.279 eV

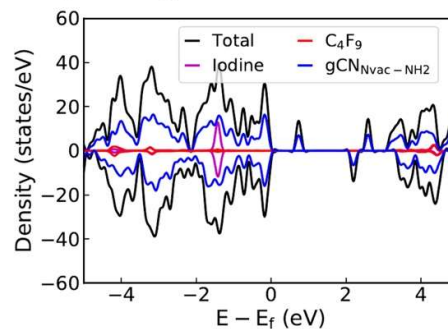


Figure SI-10: Electronic structure and the corresponding total energies of the defective gCN/C₄F₉-I with disconnected nitrogen-carbon bond cleavage on gCN surface (carbon: brown; nitrogen: blue; hydrogen: pink, fluorine: navy and iodine: magenta) at the center of the heptazine unit (structure 3.a). Calculations performed with the broken symmetry approach indicate that the ground state of this gCN form is indeed a bi-radical state.

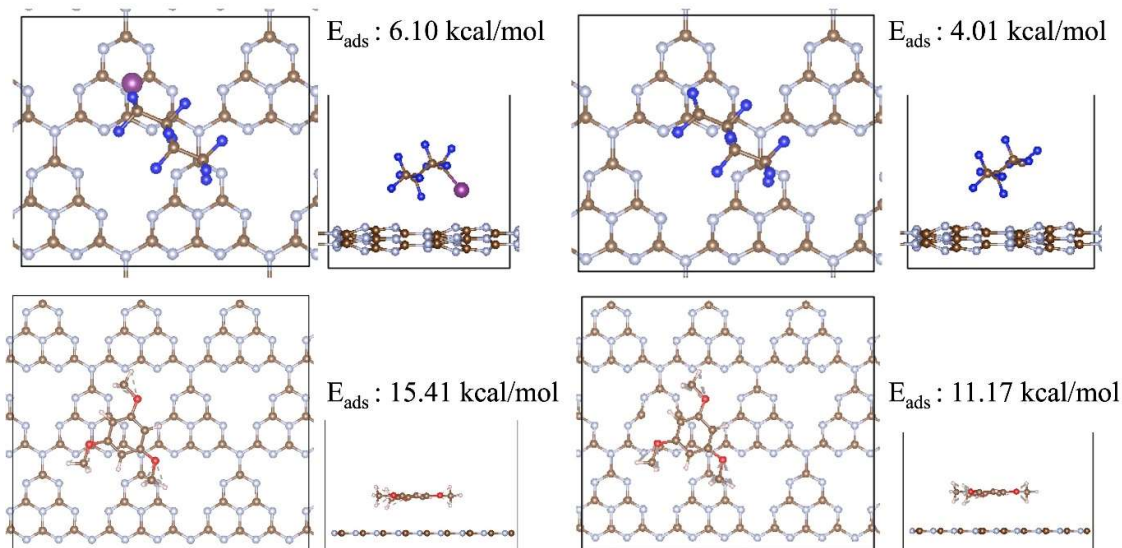


Figure SI-11: Structure and adsorption energies of (a) top-left: C₄F₉-I, and (b) top-right: C₄F₉^{*} molecules on pristine gCN surface. The adsorption energies of 1,3,5 trimethoxybenzene on (c) bottom-left: pristine gCN surface (structure P.0) and (d) bottom-right: am-gCN surface (structure 1.a) are also reported for comparison. The adsorption energy found here for trimethoxybenzene is comparable to the adsorption of phenols on the graphene surface³.

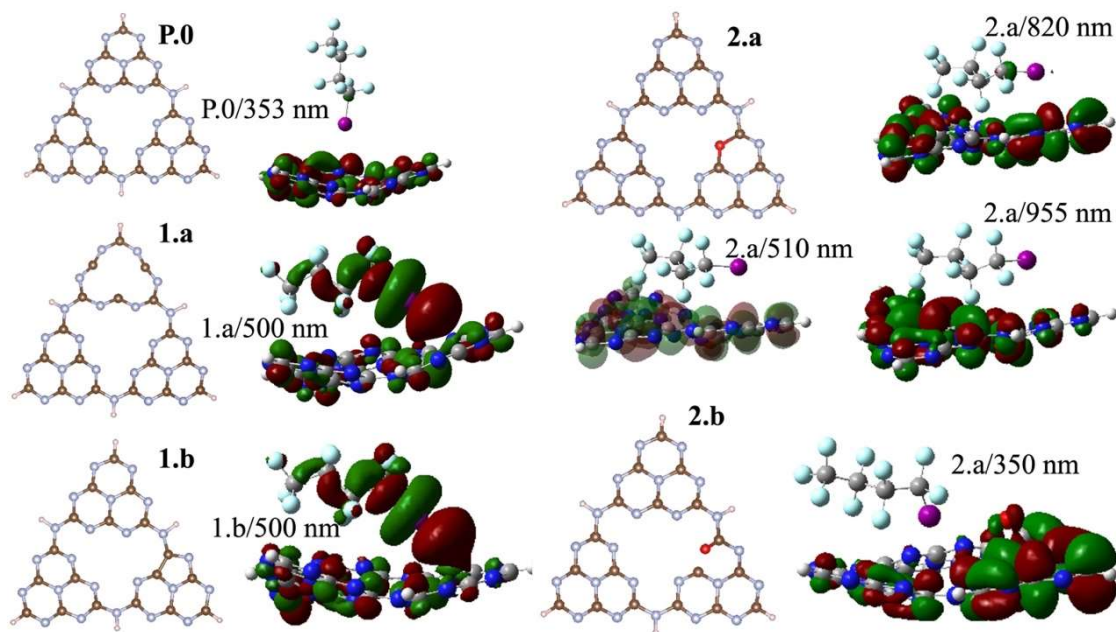


Figure SI-12: Lowest Unoccupied Transition Orbitals (LUTOs), extracted from NTO analysis, of gCN/C₄F₉-I for the gCN surface in its pristine (P.0), amorphous forms (1.a/b) and pyran-like and carbonyl-like oxygenated forms (2.a/b). Iodine and fluorine atoms of the C₄F₉-I molecule adsorbed on pristine/defective gCN units are represented with magenta and cyan colors, for clarity.

In the case of the pristine gCN surface, the LUTOs corresponding to low-energy excitations (≈ 350 nm) are confined on the semiconductor. Only with excitation at high energy (≈ 300 nm) the transition density partly spreads over the C₄F₉-I molecule (see Figure SI-8). Interestingly, for the models representing the amorphous gCN surface (structures 1.a/b) the transition densities calculated at 500 nm now show major contributions from both gCN surface *and* the C₄F₉-I molecule, in particular on the iodine atom (with a d_z^2 -like character). Such transitions are prompted by the molecule-gCN hybridization described above and involve a direct electron excitation from the localized defect state of gCN to the C₄F₉-I molecule.

In contrast, the oxygenated gCN forms do not show any electronic transition involving the unoccupied C₄F₉-I molecular orbital as landing levels (Figure 8, structures 2.a/b) but feature electron transitions occurring exclusively within the gCN surface even for the high-energy excitations (≈ 350 nm), irrespective of the pyran-like or carbonyl-like oxygenated system. In comparison, for models representing the reduced gCN surface (structures 3.a and 3.b), a small delocalization of transition density is observed on the C₄F₉-I molecule adsorbed on structure 3.a at the lowest energy excitation wavelength of ≈ 500 nm, whereas for structure 3.b, the transition density is fully localized only on the gCN surface.

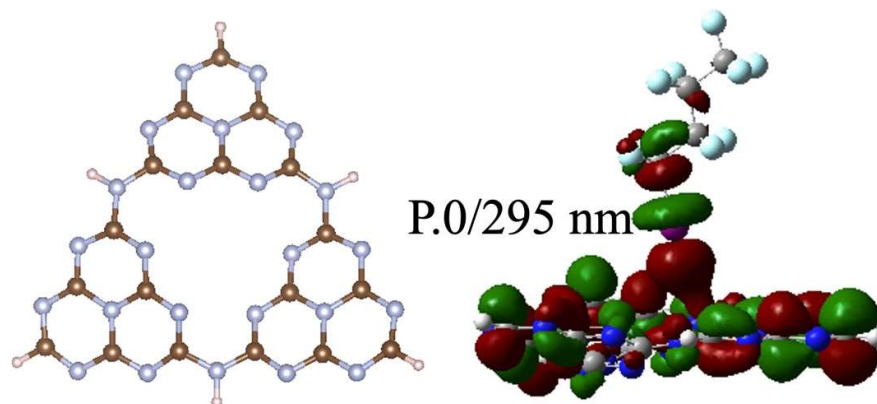


Figure SI-13: Lowest Un-Occupied Transition Orbitals (LUTOs), extracted from NTO analysis, of gCN/C₄F₉-I for the gCN surface in its pristine (P.0) form at the highest excitation energy (≈ 300 nm). Iodine and fluorine atoms of the C₄F₉-I molecule adsorbed on pristine/defective gCN units are represented with magenta and cyan colors, for clarity.

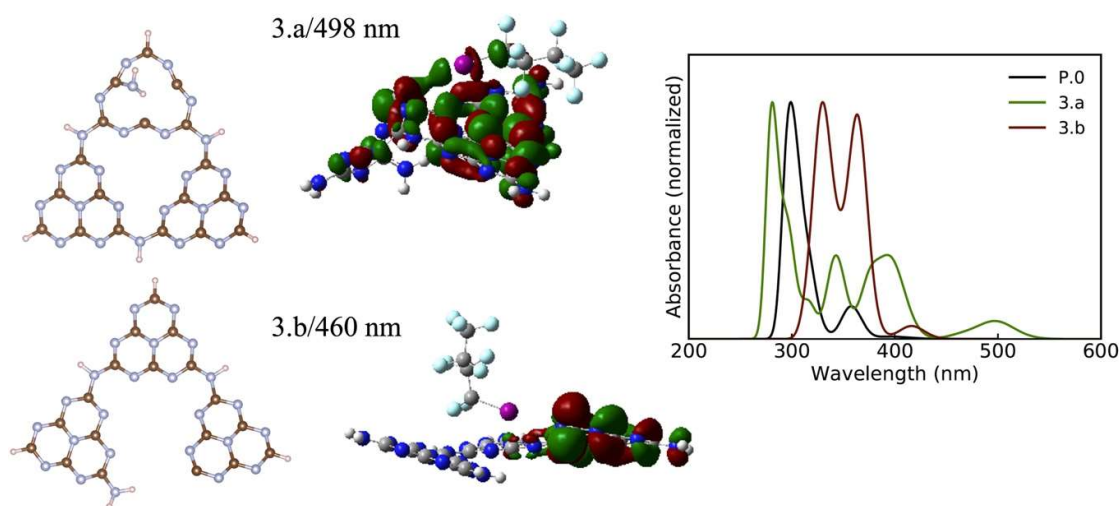


Figure SI-14: Theoretical absorption spectra (normalized) along with the Lowest Unoccupied Transition Orbitals (LUTOs), extracted from NTO analysis, of gCN/C₄F₉-I systems for gCN surface in its pristine (black curves) and defective forms; with C₄F₉-I on top of the 3.a (green) and 3.b (brown) gCN forms. Iodine and fluorine atoms of the C₄F₉-I molecule adsorbed on pristine/defective gCN units are represented with magenta and cyan colors, for clarity.

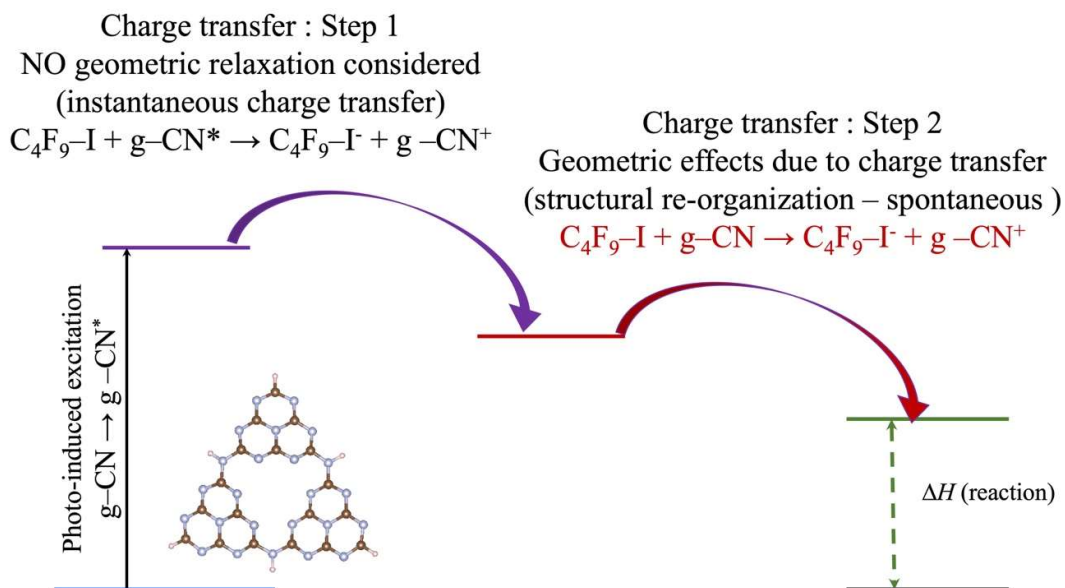


Figure SI-15: Schematic ground state charge transfer between the pristine/defective gCN surface and the associated change in reaction enthalpies.

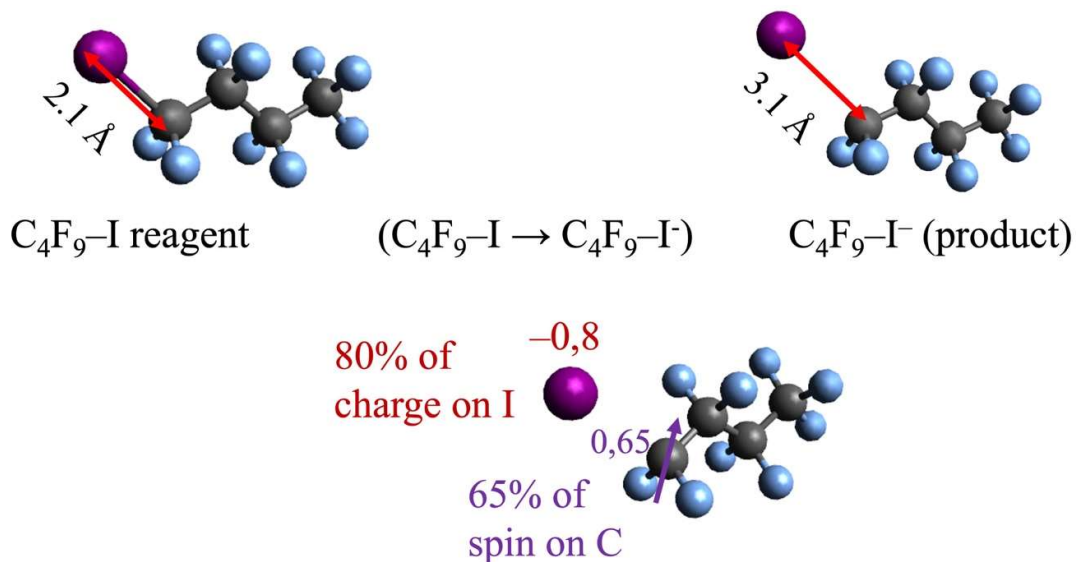


Figure SI-16: Electron/spin distribution in the C_4F_9-I molecule upon photo-induced charge transfer from the gCN surface to C_4F_9-I (bottom), under the reaction mechanism considered (top).

Table SI-3: Reaction enthalpies (ΔH) computed for the charge transfer process. ΔH is substantially lower for amorphous and reduced gCN forms (structures 1.a and 3.a), consistent with the enhanced photocatalytic response observed for these materials, experimentally.

Ref. Structure	Reaction Enthalpy (ΔH , kcal/mol) $C_4F_9-I + gCN \rightarrow C_4F_9-I^- + gCN^+$
P.0	86
1.a	25
1.b	55
3.a	25
3.b	70

References:

- (1) Höfer, P.; Grupp, A.; Nebenführ, H.; Mehring, M. Hyperfine Sublevel Correlation (Hyscore) Spectroscopy: A 2D ESR Investigation of the Squaric Acid Radical. *Chem. Phys. Lett.* **1986**, 132 (3), 279–282. [https://doi.org/10.1016/0009-2614\(86\)80124-5](https://doi.org/10.1016/0009-2614(86)80124-5).
- (2) Stoll, S.; Schweiger, A. EasySpin, a Comprehensive Software Package for Spectral Simulation and Analysis in EPR. *J. Magn. Reson.* **2006**, 178 (1), 42–55. <https://doi.org/10.1016/j.jmr.2005.08.013>.
- (3) Avila, Y.; Coccoletzi, G.H.; Romero, M.T. First principles calculations of phenol adsorption on pristine and group III (B, Al, Ga) doped graphene layers. *J Mol. Model.* **2014**, 20, 2112. <https://doi.org/10.1007/s00894-014-2112-0>